Experimental investigation of the flow characteristics within a vortex tube with different configurations

Experimental investigation of the flow characteristics within a vortex tube with different configurations

Yunpeng Xue[a,b], Jonathan R. Binns[a], Maziar Arjomandi[c], & Hong Yan[b]

[a]National Centre for Maritime Engineering and Hydrodynamics, Australian Maritime College, University of Tasmania, Australia.

[b] School of Power and Energy, Northwestern Polytechnical University, Xi'an, China.

[c] Mechanical Engineering, University of Adelaide, Adelaide, Australia.

Abstract

The energy separation in a vortex tube is a combined result of different factors and its explanation remains debatable. As a classical fluid mechanics phenomenon, understanding of the complex helical flow mechanism within a vortex tube is a necessary foundation. The small scale of an industrial vortex tube and the extremely complex flow conditions are the two main challenges in obtaining the internal flow properties. This paper reports the results of an experimental investigation on the flow behaviour within a confined cylindrical system having different configurations corresponding to the actual flow field in a vortex tube at different conditions. Transparent devices were used to enable flow visualisation and Particle Image Velocimetry (PIV) measurement. The results of the flow visualisation and PIV experiments show that a precessing vortex core is significant only in a specific range of swirling strength. A good agreement between the observed flow characteristics and previously published results was observed.

1. Introduction

A vortex tube is a simple thermal device that can separate a single injection of compressed gas into two streams of different temperatures. As shown in Figure 1, a typical counter-flow vortex tube consists of a tangential inlet, a central cold nozzle and a peripheral hot exit. Once the compressed gas is injected into the tube tangentially, it forms a strong swirling flow. Due to the tube structure, two streams emanate from the central nozzle near the injection and the peripheral gap at the other end of the tube. The two exhausts are defined as cold flow and hot flow because of their temperature difference from the inlet temperature, respectively.

Compared to conventional thermal devices the vortex tube has many advantages: no moving parts, no electric or chemical elements, lightweight, low in cost, maintenance free, instant cold and hot air, and adjustable temperatures [1]. These advantages make the vortex tube an attractive device for instant cooling [2-4], dehumidification [5], mixture separation [6] and other applications [7]. Since its invention, different explanations for the energy separation phenomenon of a vortex tube have been proposed, but none is well-accepted due to lack of high-fidelity experimental data [7-11].

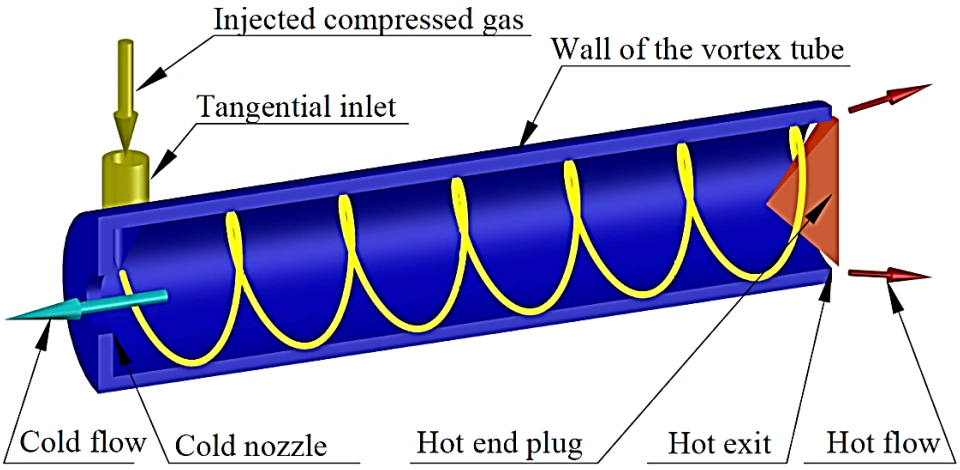

Figure 1. Structure of a typical counter-flow vortex tube and the internal dominating flow structure

The performance of a vortex tube is a complex result of several factors, such as tube geometry, inlet and outlet conditions, and working fluids. A detailed discussion of these factors has been reported [12, 13]. For a certain vortex tube, the energy separation is only caused by the strong swirling flow. Therefore, to be able to explain the energy separation phenomenon in a vortex tube, it is important to understand the underlying mechanisms and flow features inside the vortex tube. To investigate this flow mechanism, Xue et al., visualized the flow in a water-operated vortex tube [14]. They presented a qualitative analysis of the flow characteristics which significantly contributed to the understanding of the flow mechanism and energy separation process within the vortex tube. The high-fidelity measurement of the flow properties within a vortex tube is very challenging due to the small dimensions of a typical tube (diameter of 10 *mm*) [15] and the strong swirling flow (angular frequency of up to 10^6 Hz has been estimated) [16]. Therefore, large scale vortex tubes have been used to obtain detail information of the internal flow mechanism. Pressure, velocity and temperature profiles in such large tubes were measured by Hartnett [17] and later by Lay [18, 19] and Bruun [20]. In another study, Takahama reported the existence of a forced vortex and

measured its swirl velocity [21]. The existence of a secondary flow in a vortex tube was explained and demonstrated by the measurement of both tangential and axial velocity components within a vortex tube by Ahlborn and Groves [22]. In their work, the swirl velocity distribution was measured and described as a Rankine vortex, consisting of a forced vortex in the centre and a free vortex in the periphery. Further on, Gao [16] reported 3-D velocity distribution of the internal flow measured in a 2.5 meter-long vortex tube. A forced vortex was reported through the whole tube except in the vortex chamber where a Rankine vortex was observed. Xue et. al., measured the 3-D velocity profiles within a large scale vortex tube focusing on the radial component and turbulence intensity [23]. It was found that the radial velocity, which had been considered negligible in previous studies, was an essential component of the flow structure inside a vortex tube. They also found that in the central region of the tube, the free vortex at the hot end was transformed to a forced vortex near the injection, and energy is transferred from the central to the peripheral zone in this process [24]. The vortex breakdown and the precessing vortex core (PVC) in a vortex tube were investigated in recent numerical simulations [25, 26]. The oscillation of the boundary was reported as the primary mechanism for energy transfer. They also reported a different statement of the axial stagnation point location in a vortex tube as a function of the cold mass fraction from previous experimental and analytical work [13, 16].

In all of the previous measurements of the flow properties within the vortex tube, an intrusive technique was used where a probe was inserted into a large-scale tube, hence resulting in an induced disturbance of the flow. The strong turbulence and lack of information about the flow direction in the central region of the tube imply the requirement of a nonintrusive technique for collection of a high-quality and accurate measurement data-set. For the first time, Liew et al. attempted to measure the velocity within a vortex tube using an optical method [5, 27, 28]. In their LDA (Laser Doppler Anemometry) experiments, water droplets were used as seeding particles. Water was sprayed through a high-pressure nozzle to generate small droplets with the mean diameter of about 10 μm. Effective measurements of the velocity profile were performed only near the inlet of the vortex tube due to the strong swirling of the flow. Two other issues in the measurement process were reported in their studies, i.e., the Stokes number and evaporation of the water droplets. Based on the droplet dimension and the inlet velocity, the Stokes number at the inlet was estimated, which could exceed 1. This implied that the particles did not follow the flow properly and the accuracy of the measurement results remained debatable. The second issue was the short lifetime of the

water droplet. It was noticed that the droplets evaporated after a short distance from the injection (about 0.1L from the injection, here L is the total length of the tube) and an LDA measurement was only possible in this very specific location of the tube.

The different configuration of a vortex tube system causes different flow feature within the tube and hence results in different working performance. To date, there are only a few studies on the velocity characteristics of the swirling flow in a vortex tube with different configurations. A better understanding of the internal flow mechanism is still required in order to effectively explain the separating processes in the tube and improve the tube performance. This paper reports the results of an experimental study focusing on the swirling flow structure inside a confined water-operated vortex system that corresponding to the vortex tube with different configurations using the Particle Image Velocimetry (PIV) and flow visualisation techniques. The results of the experiments give important insights into the underlying flow behaviour inside the vortex tube.

2. Methods and apparatus

2.1. The vortex tube

To enable PIV measurement and flow visualisation within the vortex tube, transparent acrylic tubes were used. Figure 2 shows the configuration of a typical vortex tube used in this research, including the variable parameters. Two tangential nozzles were located at one end of the tube to allow the injection of fully developed turbulent flow which was notified by the inlet velocity and the nozzle configuration. A 5 *mm* central nozzle was positioned near the injection port to form the cold exit and a 1 *mm* peripheral gap was used at the other end of the vortex tube as the hot exit. It should be noted that there is negligible temperature change in the current experiments and hence the cold exit and hot exit in this work are only named for a consistency in the field. The effects of the flow condition and tube configurations on the working performance of a vortex tube have been systematically discussed in previous research [13]. In order to have comparable results, different configurations were selected in this work for a systematic investigation of the characteristics of the internal swirling flow (Figure 3). Key parameters of these configurations are summarised in Table 1.

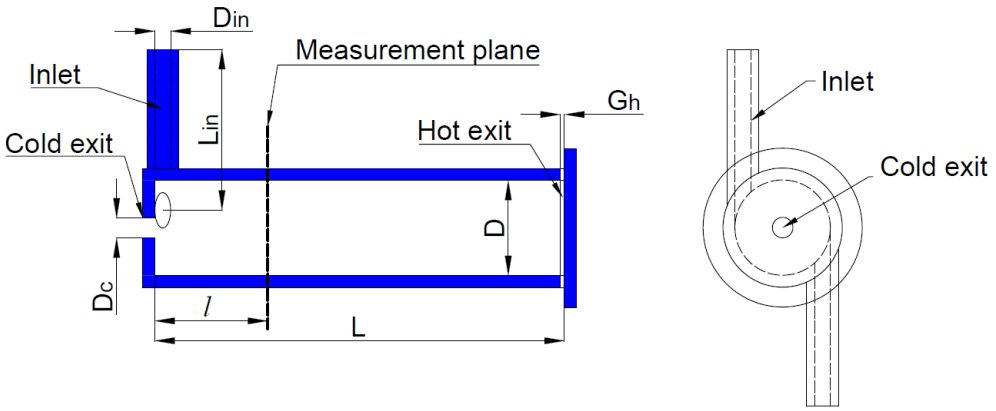

Figure 2. The schematic of the vortex tube used in this work for PIV experiments (details are listed in table 1).

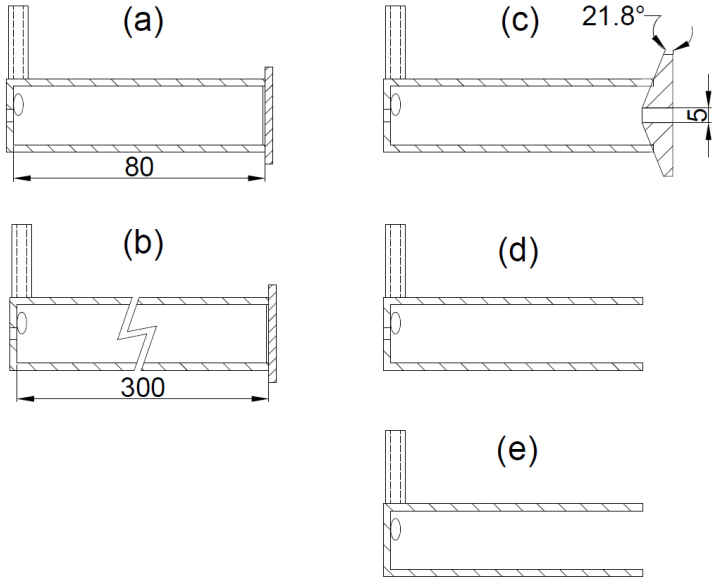

Figure 3. Different configurations of the investigated tubes used in current work (dimension in mm).

Table 1. Key parameters of the investigated tubes in the current work.

	Key parameters of the tube						
Model	Length (L), *mm*	Diameter (D), *mm*	Inlet length (L_{in}), *mm*	Inlet diameter (D_{in}), *mm*	Cold nozzle diameter (D_c), *mm*	Hot exit gap (G_h), *mm*	Measurement location,*l/L*
(a)	80	30	50	5	5	1 (peripheral)	$\frac{N}{8}$, *N=1, 2, 3, 4, 5, 6, 7, 7.8*
(b)	300	30	50	5	5	1 (peripheral)	$\frac{2N-1}{30}$, *N=1,2, 3, …, 15*
(c)	80	30	50	5	5	5 (diameter, central)	$\frac{N}{8}$, *N=1, 2, 3, 4, 5,*

(d)	80	30	50	5	5	30 (fully open)	$\frac{N}{8}$, *N=1, 2, 3, 4, 5, 6, 7, 7.8*
(e)	80	30	50	5	0 (closed)	30 (fully open)	$\frac{N}{8}$, *N=1, 2, 3, 4, 5, 6, 7, 7.8*

2.2. Experimental arrangement and PIV setup

The experimental campaign was performed at a standard room temperature and pressure using water as the working fluid. The difference in the fluid compressibility in the current work is noticed. The similarity of the flow structure in air/water-operated vortex tube [14, 29] and gas/liquid-cyclone [30-32] supports the usage of incompressible water and the results from this work will also be compared with previously published experimental data in an air-operated vortex tube for further validation and analysis. In the entire experiment, the tube was fully submerged in a rectangular transparent water tank to reduce the influence of ambient pressure and gravity on the working fluid. Water was pumped into the tube via the tangential inlets from a round pipe with a length-to-diameter ratio of 10 to ensure fully-developed flow conditions at the inlet. The total inlet volume flow rate was set at 3.4 *L/min*, which resulted in an inlet jet velocity of v_{in} = 1.4 *m/s* and an inlet jet Reynolds number of 7000. The water discharged from the outlets was recirculated back into the water tank, resulting in a closed system, as shown in Figure 4.

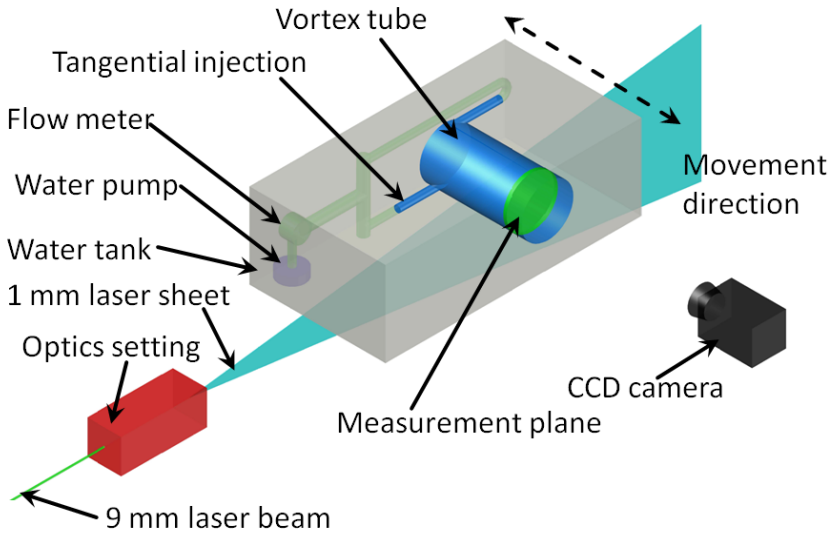

Figure 4. Experimental arrangement for the PIV measurement and flow visualisation.

Particle Image Velocimetry (PIV) was used to measure the instantaneous and mean velocity

field within the tubes. The flow was seeded with hollow spherical glass with a mean diameter of d_p =10 μm and a specific gravity of γ=1.05. The resultant characteristic Stokes number was $Stk \approx 10^{-5}$, which is sufficiently low to enable the particles to faithfully follow the flow down to the smallest scales which can be resolved by the PIV measurement. As the experimental arrangement was a closed system, continuous seeding of particles was not required.

The source of illumination for the PIV experiments was a 532 *nm* Nd-YAG double-pulsed laser, which was used to generate a 1 *mm* thick laser sheet. PIV images were recorded using a Kodak Megaplus ES2093 CCD camera, with a spatial resolution of 1920×1080 pixels. Multiple measurements were performed at different axial locations along the tube as shown in Figure 2. For each measurement station, a minimum of 100 PIV image pairs were recorded. To obtain these parallel sheets, the laser and the optics were kept stationary and the entire experimental system, including the water tank, was shifted precisely using a mechanical traverse. Optical distortion in the PIV measurement was minimised by the complete submersion of the tube in water and the subsequent selection of acrylic, which has a similar refractive index to that of water (1.49 and 1.33, respectively), as the construction material for both the tube and the water tank. Any remaining optical distortion was corrected during post-processing of PIV images. This was done by first computing the spatial distortion in an image of a square grid that was inserted into the reactor prior to the experiment and then applying an inverse-distortion transformation to the recorded images. The PIV vectors were calculated using a 32 by 32-pixel interrogation window (IW) size with a 50% overlap. The mean particle seeding density was approximately 20 particles per IW. To maintain sufficient particle pairs within the IW, the laser pulse time delay was reduced which resulted in an in-plane particle displacement of about 2 pixels. Using an estimated PIV sub-pixel accuracy of 0.1 pixels [33], the maximum error in the measurement of instantaneous velocity was calculated to be 5%. For the 30 *mm* tube, the flow field was recorded at about 600 × 600 PPI with the equivalent resolution being about 5 μm, which ensures the successful capture of the displacement of the vortex centre. The overall flow field within the vortex tube was also visualized employing hydrogen bubbles and air bubbles. A video camera (frame rate of 30 *fps*, resolution of 3648×2736) was used to provide still and video recordings of the bubble-laden flow.

3. Results and analysis

3.1. Swirl velocity profile in the tubes

Figure 5 presents a time-average velocity vector field of the internal flow (a) and its velocity profiles normalized by the inlet velocity ($U=u/v_{in}$, $V=v/v_{in}$, $I=(u^2_{rms}+v^2_{rms})^{0.5}/v_{in}$) along the centreline (b) within the tube "a" at l/L=0.75. As can be seen, the flow along this plane is predominantly structured as a vortical flow. The swirl velocity profile reveals a Rankine vortex in the tube and reaches a maximum of 0.43 at $|r/D|\approx$0.42. The boundary flow is clearly shown by the sharp decrease of the swirl velocity and the increased turbulent intensity near the wall. The non-zero radial component of the velocity profile indicates the complexity of the vortex flow and existence of three-dimensional flow structure. One of the most significant features of the flow is the strong turbulence in the central region, with a turbulent intensity up to about 20%. Considering the small magnitude velocity profile in the central region, this strong turbulence indicates the existence of a precessing vortex core. The oscillation of the vortex core around the centre represents a strong fluctuation of the flow velocity and regular change of the flow direction near the centre, hence results in a strong turbulent flow. The existence and effects of the precessing vortex core will be further discussed later.

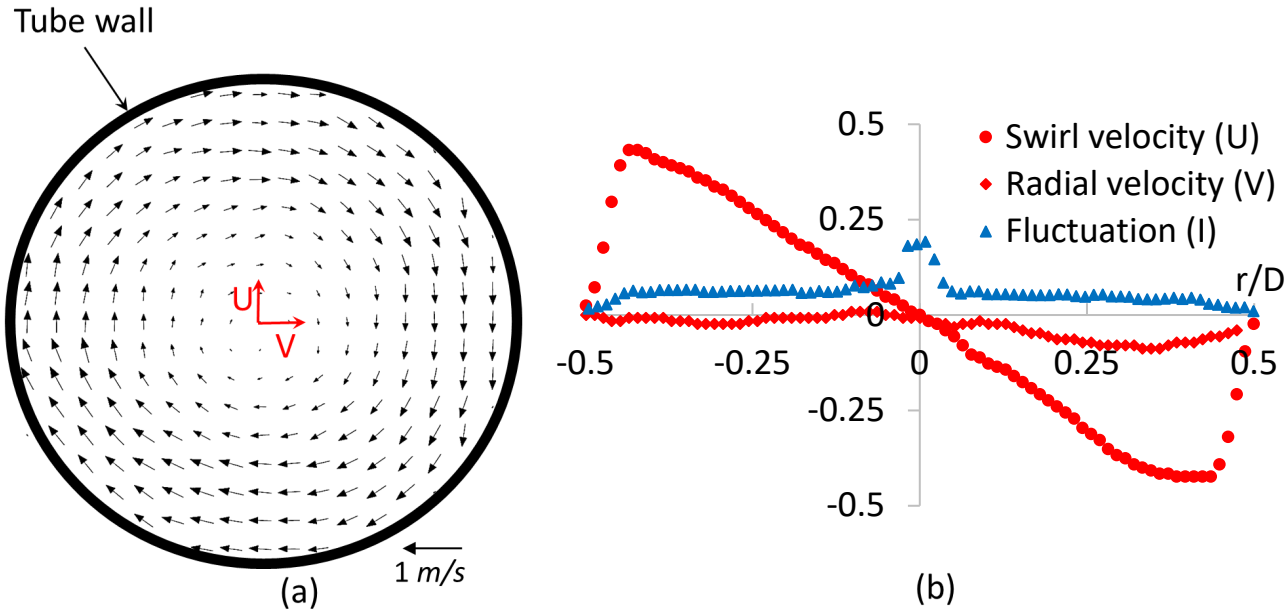

Figure 5. A typical PIV velocity vector field (a) and its velocity distributions along the centreline in tube "a" at l/L=0.75 for the condition of v_{in} = 1.4 *m/s* (b).

Figure 6 presents the normalized time-averaged swirl velocity ($U=u/v_{in}$), in the short vortex

tube (case "a") at different axial locations. The velocity data are plotted against the radial locations normalized to the tube diameter, *r/D*. From Figure 6, it can be observed that the swirl velocity of the flow within the tube does not change significantly with the axial location, although there is a relatively small reduction towards the hot end. A major flow feature in the tube can be characterised as a Rankine vortex, with a "forced" vortex in the core within the region of $|r/D| \leq 0.45$, surrounded by the boundary layer flow. The swirl velocity reaches a maximum at $|r/D|=0.45$ in the front part of the tube, i.e., $l/L \leq 0.625$.While, in the rear part of the tube, the flow is further developed and the maximum velocity reduces to 0.42 and 0.36 at $l/L=0.75$ and $l/L=0.975$, respectively.

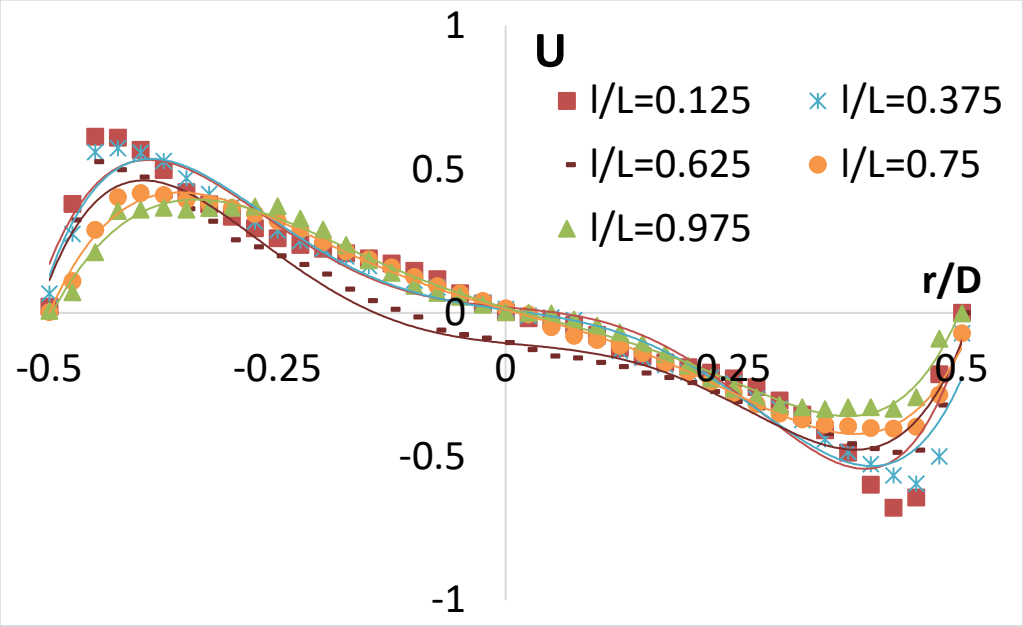

Figure 6. Non-dimensional swirl velocity distribution along the short vortex tube (case "a"), normalized by inlet velocity.

The development of the boundary layer flow is noted from the velocity profiles and estimated using the following relationship [34] as:

$$k_s^+ = \frac{u_{\tau,Max} k_{s,Max}}{v} \approx \frac{2 \times 0.1 \times 5 \times 10^{-6}}{1 \times 10^{-6}} = 1 \lesssim 4$$

Here, k_s^+ is the Roughness Reynolds Number, $u_{\tau,Max}$ is the maximum friction velocity within the tube, estimated as 10% of the maximum velocity (2 *m/s* for case "c"), $k_{s,Max}$ is the estimated maximum characteristic roughness of the tube (0.005 *mm*), v is the kinematic viscosity. Therefore, the flow within the vortex tube can be considered to be hydraulically smooth for $k_s^+ \lesssim 4$ and the effect of surface roughness is negligible in this work. As presented in the figure, the thickness of the boundary flow increases from 0.05 D (1.5 *mm*)

near the injection to 0.075 D (0.225 *mm*) near the hot end. The velocity gradient of the boundary layer flow that indicated by the slope of the swirl velocity in boundary layer ($0.45 \leq |r/D| \leq 0.5$) decreases by 63.7% from l/L=0.125 to l/L=0.975. The velocity profile at l/L=0.625 is particularly interesting, as it shows an offset of the flow centre from the geometrical centre of the tube. This implies the existence of a vortex precession in the tube which will be discussed later. The normalised radial velocity presented in Figure 7 indicates the small magnitude of the radial component along the tube (except at l/L=0.125), which was always ignored in previous research [11]. The negative radial velocity at l/L=0.125 indicates the inwards flow from the peripheral layer to the central region.

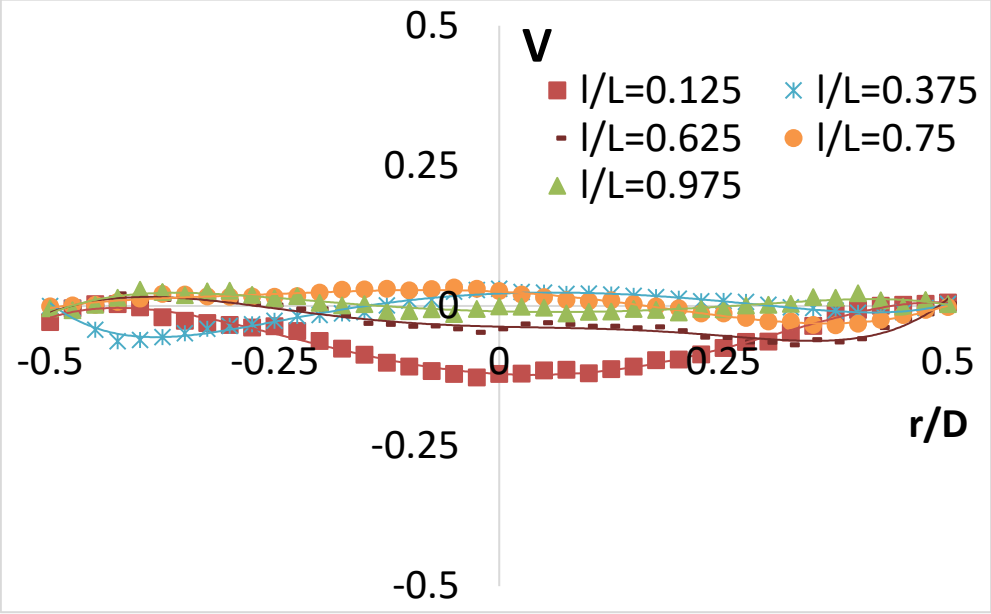

Figure 7. Non-dimensional radial velocity distribution along the short vortex tube (case "a"), normalized by inlet velocity.

The normalized swirl velocity profile along the long vortex tube (case "b") is presented in Figure 8. Comparing to the flow in the short tube (case "a"), several common flow features can be seen which are summarized as follows. Firstly, the maximum swirl velocity decreases from 0.614 to 0.598 for the same inlet velocity. Secondly, the boundary layer flow pattern can be clearly seen in the figure indicated by the sharp drop of the velocity profile near the wall. Indeed, similar boundary layer flow behaviour was observed in all different cases in this work. Thirdly, as shown by the non-zero velocity profiles along the tube centreline, the position of the vortex core does not coincide with the geometrical centre of the tube. As the tube is 2.75 times longer than the first case, different flow behaviour is also noted. The most significant feature is the transformation from a forced vortex at the injection to a free vortex near the hot end, which has been reported in the air-operated vortex tube [23, 24] (Figure 14

(a)). It is worthwhile to note that the precessing of the unsteady vortex core in the long tube is more significant than that in the short tube. Presented in Figure 9, the radial component of the swirling flow shows the outwards movement of the central flow at *l/L*=0.767, which indicates the existence of the multi-circulation hypothesised in a previous investigation [13].

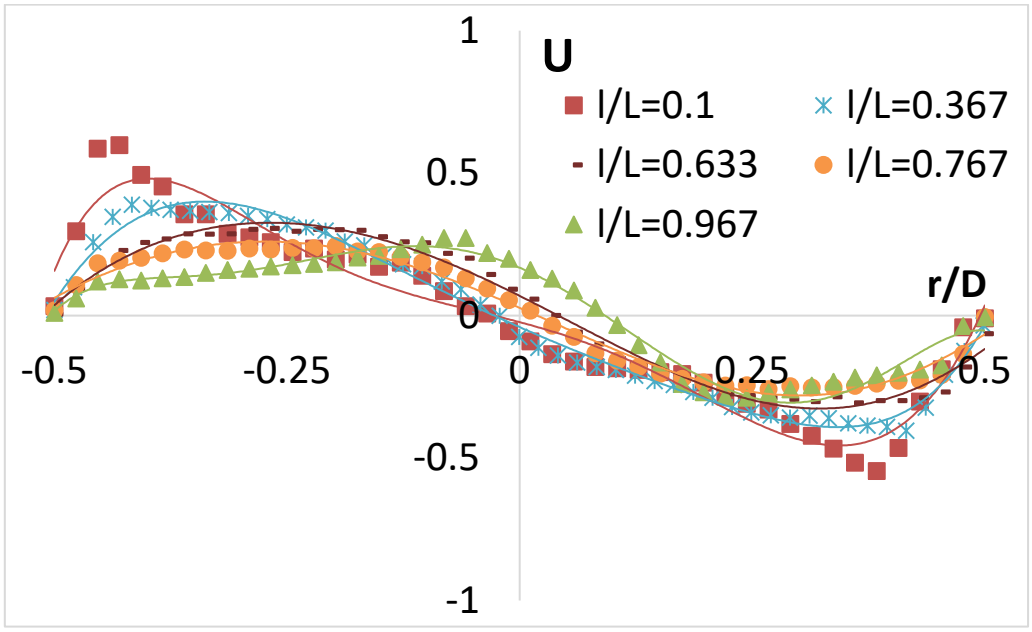

Figure 8. Non-dimensional swirl velocity distribution along the long vortex tube (case "b"), normalized by inlet velocity.

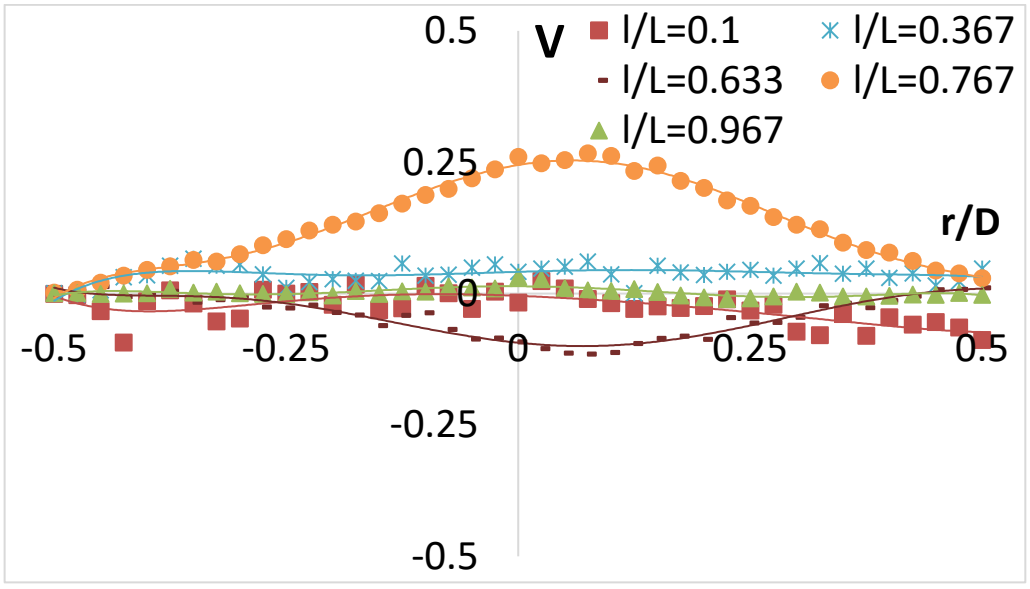

Figure 9. Non-dimensional radial velocity distribution along the long vortex tube (case "b"), normalized by inlet velocity.

The swirl velocity profile in case "c" presented in Figure 10 shows different flow features from the first two cases. Due to the optical limitation in this case, i.e., the conical plug, the effective measurement was not available in the rear part of the tube, i.e., near the hot end. In

contrast to the previous cases, the most significant flow feature within the tube is the dominating free vortex. This dramatic difference is caused by the different geometry of hot end plug. The cold mass fraction is an important parameter in the investigation of vortex tube and is defined as the ratio of the cold mass flow rate over the inlet mass flow rate. This fraction in case "c" is approximately 0.5, which is much greater than that in the previous two cases, i.e., 0.17. Furthermore, at l/L=0.625, the maximum swirl velocity in the central region of the tube reaches about 1.4 in the central region of the tube. This implies the injected flow was accelerated inside the tube due to the blockage of the hot end plug as described in [13]. It is also found that the maximum swirl velocity at the different measurement planes decreases towards the inlet. Hence, it is reasonable to predict that the maximum swirl velocity can be observed near the hot end of the tube.

Based on the velocity profile, the internal flow feature near the hot end can be explained as follows. As mentioned in previous discussion [13], the peripheral swirling flow moves from the injection point to the hot end and as it reaches the plug it is forced back through the central region of the tube due to the blockage of the hot end plug. As the rotation radius decreases at the plug, the swirl velocity increases to preserve the mass flow rate, hence it results in the formation of a free vortex. The dominating free vortex within the tube, the acceleration of the injected fluid and the reduction of the swirl velocity towards the inlet are in a good agreement with the flow feature within vortex tubes with large cold mass fraction [23, 24, 35] and cyclones [36-38]. Moreover, the velocity profile in the central region also shows that a strong precessing vortex core does not exist in this case.

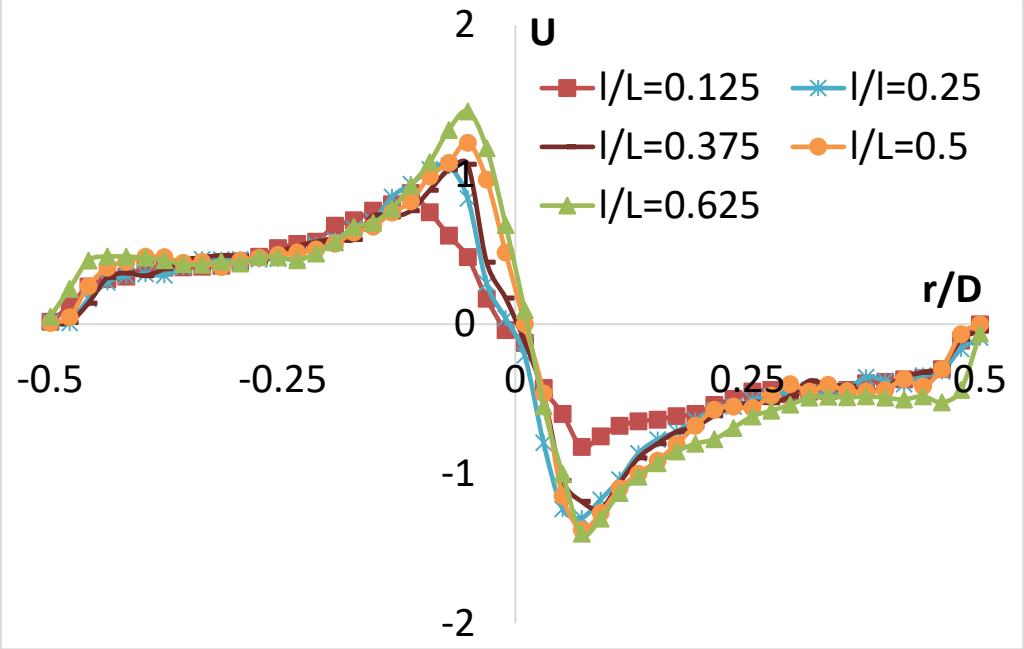

Figure 10. Non-dimensional swirl velocity distribution along the tube (case "c"), normalized by inlet velocity.

Figure 11 and 12 show the swirl velocity profiles in case "d" and case "e", respectively. As the hot end of the tubes were fully opened, the tube "d" and tube "e" behave very similar to a vortex tube at negative or zero cold mass fraction, respectively. These two figures clearly present some distinctive flow features, including the deceleration of the peripheral flow, the thickening of the boundary layer from the inlet towards the hot end, and the acceleration of the central fluid, which are mainly caused by the flow viscosity. Figure 13 compares the velocity profile at different positions in the tube "d" and "e". It is clearly shown that there is a negligible difference between the flow patterns in the front part of the two tubes. While, in the rear part of the tube, the swirl velocity in case "d" has a greater decrease such that the maximum velocity at l/L=0.975 is approximately 20% slower. As the fluid flows towards the hot end, the swirl velocity decreases because of the friction. The existence of the central hole in case "d" enables the suction of ambient fluid, which then flows to the other end of the tube. This induced extra mass in the central region leads to a greater decrease of the swirl velocity in the rear part of the tube in case "d" to keep the constant momentum. This suction from the central hole agrees well with the extreme operational condition of the air-operated vortex tube reported in [13, 23], i.e., suction of ambient air from the cold nozzle.

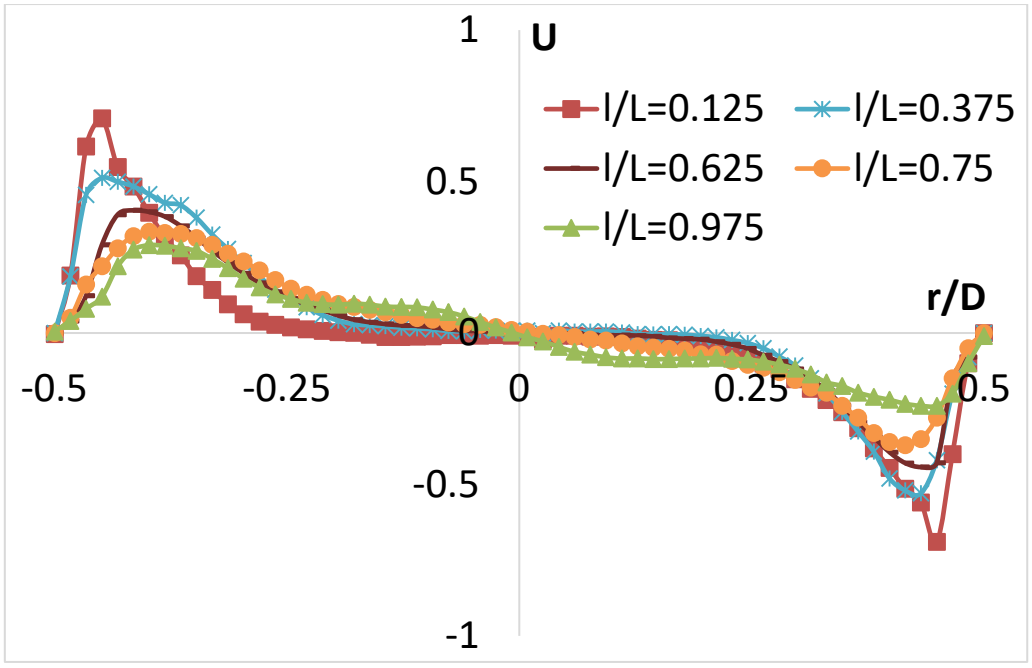

Figure 11. Non-dimensional swirl velocity distribution along the tube (case "d"), normalized by inlet velocity.

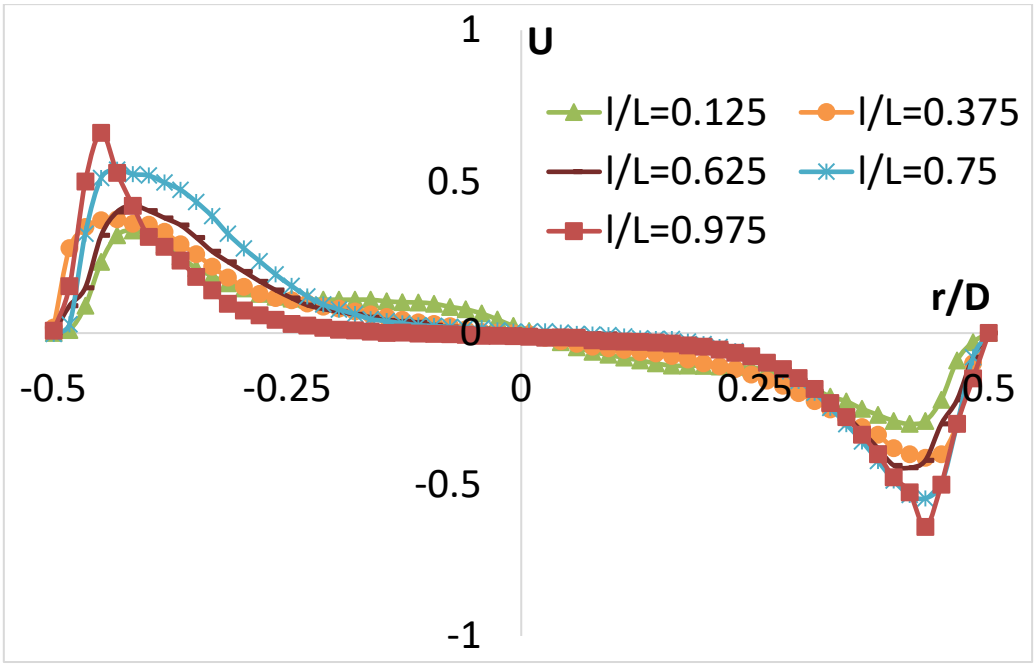

Figure 12. Non-dimensional swirl velocity distribution along the tube (case "e"), normalized by inlet velocity.

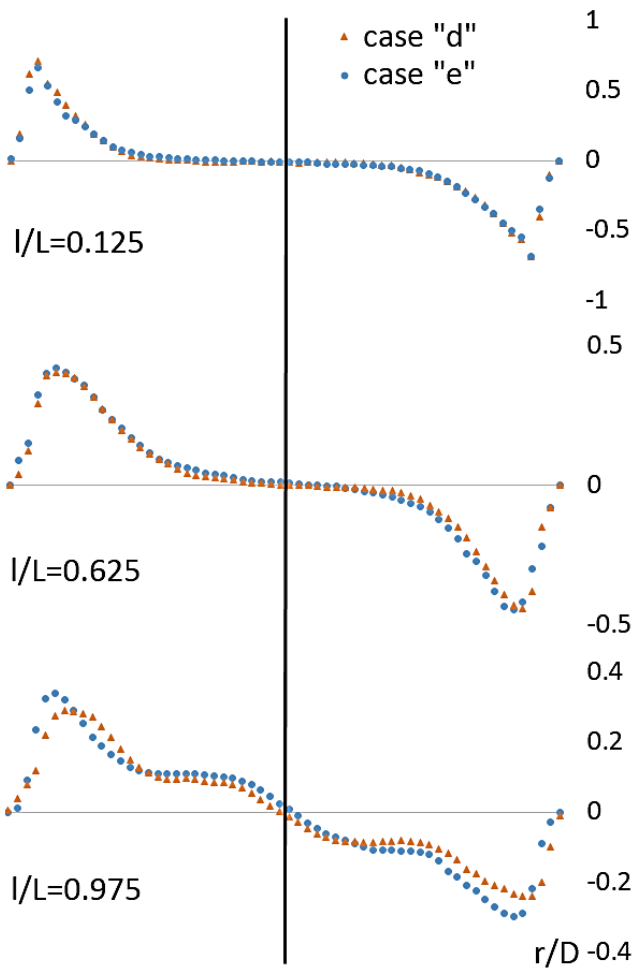

Figure 13. Comparison of the nondimensional swirl velocity profiles in the tube "d" and "e".

Presented in Figure 14, the normalized swirl and radial velocity distributions in a long air-operated vortex tube (L/D=21) enable comparisons between the current work and previous experimental results [23, 24]. A good similarity of the main flow pattern in the water-operated vortex tube and an air-operated vortex tube is observed. Dominating forced vortex in the central part is found all along the short vortex tube (case "a", Figure 6), while transformations from a forced vortex near the injection to a free vortex near the hot end are shown in long vortex tubes (case "b", Figure 8 and Figure 14 (a)). In the short vortex tube (Figure 7, L/D=2.6), the inwards flow that indicated by the negative radial velocity is significant in the central region, while in the long vortex tubes (Figure 9 and Figure 14 (b), L/D=10, 21 respectively) the inwards flow are found significant in the peripheral region. Another similar flow feature in the long vortex tube that presented by the positive radial velocity in the rear part is the outwards flow from the central to the peripheral region which indicates the existence of the multi-circulation (Figure 9 and Figure 14 (b)). Corresponding to a large cold mass fraction in previous discussion [13], the flow feature in case "c" indicates the

dominating free vortex near the hot end and hence results in a smaller scale of the multi-circulation. The existence of the suction of ambient fluid in case "d" and its effect on the flow feature comparing with case "e" agree well with the flow mechanism within a vortex tube at a small cold mass fraction as discussed in [13]. Therefore, the observed flow features in different cases are consistent with the proposed flow mechanism in a vortex tube at different conditions and hence provide further support to the hypothesis.

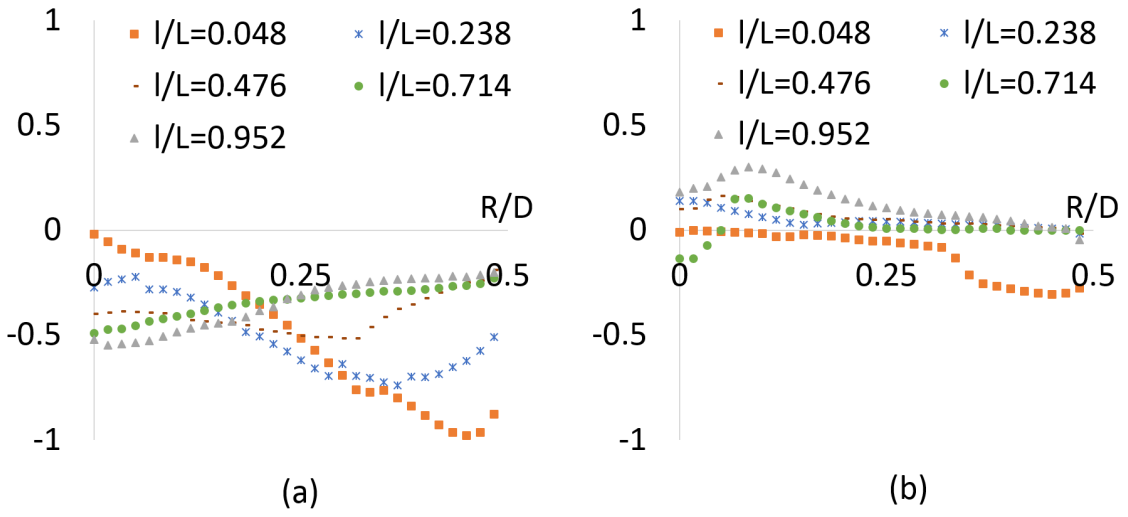

Figure 14. Non-dimensional swirl (a) and radial velocity (b) distribution along the air-operated vortex tube reported in [23], normalized by the inlet velocity.

3.2. The vortex precession in the cavity

As mentioned above, the offset between the vortex centre and the geometrical centre of the tube observed in both the instantaneous and average swirl velocity datasets can be attributed to the formation of the vortex precession. It has been reported that the precessing vortex core (PVC) contributes to the energy separation in Kurosaka's experiment [39]. A vortex core has previously been defined as the reverse flow in the axial direction or the forced vortex flow of a Rankine vortex in previous investigations [40]. In this work, the vortex core is defined as the centroid of the vortex flow that is oscillating around the geometrical centre.

Flow visualisation was used to identify several key features of the flow structure within the tube. These features were identified based on both "still" images and video recordings of the flow. From video recordings of the flow, it was observed that the vortex oscillates unstably around the geometrical centre of the tube, which proves the existence of a Precessing Vortex Core. Figure 15 presents three consecutive frames of the visualized vortex core from a video recording (at 30 *Hz*). Due to the centrifugal force, the continuously generated hydrogen

bubble at the hot end (case "b", $l/L \approx 0.975$) concentrates in the core of the swirling flow. Because of the continuous hydrogen generation, the visualized vortex core grows, which is indicated by the "cloud" in the images. The clockwise oscillation of the vortex core is clearly shown in this figure and the precessing frequency of this vortex core was estimated to be approximately 2 *Hz* from the video recording. According to the velocity profile at the hot end presented in Figure 8, the angular velocity of the vortex core at l/L=0.975 is about 12.2 *rad/s*, which gives the precession frequency of 1.94 *Hz* which demonstrates a good agreement between the visualisation and PIV measurement.

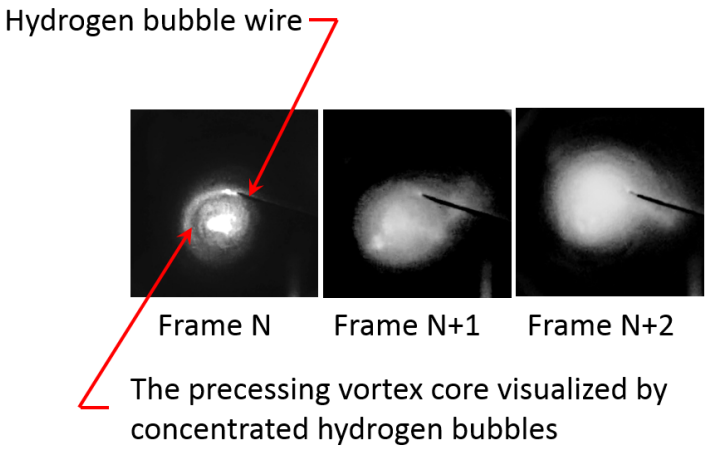

Figure 15. Three continuous frames from the video recording of the visualized precessing vortex core by the concentrated hydrogen bubbles at the hot end plug (case "b", $l/L \approx 0.975$).

The precessing vortex core in a vortex tube was firstly studied numerically in recent work [25, 26], its existence and effects on separation have been discussed. The iso-surface of the instantaneous axial velocity was used to show the flow structure of the vortex core as shown in Figure 16 (a). Figure 16 (b) and (c) are two images taken by the Kodak Megaplus camera showing the oscillating vortex core in case "b" and "c" using concentrated hydrogen bubbles and air bubbles, respectively. Hydrogen bubbles were generated by a short wire at the centre of the hot end and moved towards the cold end through the central region of the tube. The concentrated bubbles clearly indicate the existence of the PVC in the tube, except the region near the cold end due to the dissipation of the bubbles and decrease of the swirl velocity of the central flow (Figure 16, (b)). Due to the tube structure in case "c", air bubbles were introduced through the hot nozzle. The concentrated air core, in this case, is very stable, hence implies a weak precession of the vortex core. This observation agrees well with the swirl velocity profile reported in Figure 10. The existence of the PVC, which is a three-dimensional, unsteady quasi-periodical fluid-dynamic instability, helical in nature, within the

current cavity has also been observed in other similar cavities [13, 14, 40-43]. This implies that the PVC is a common flow characteristic in a vortex flow and fundamental research on the nature of precessing vortex core is recommended.

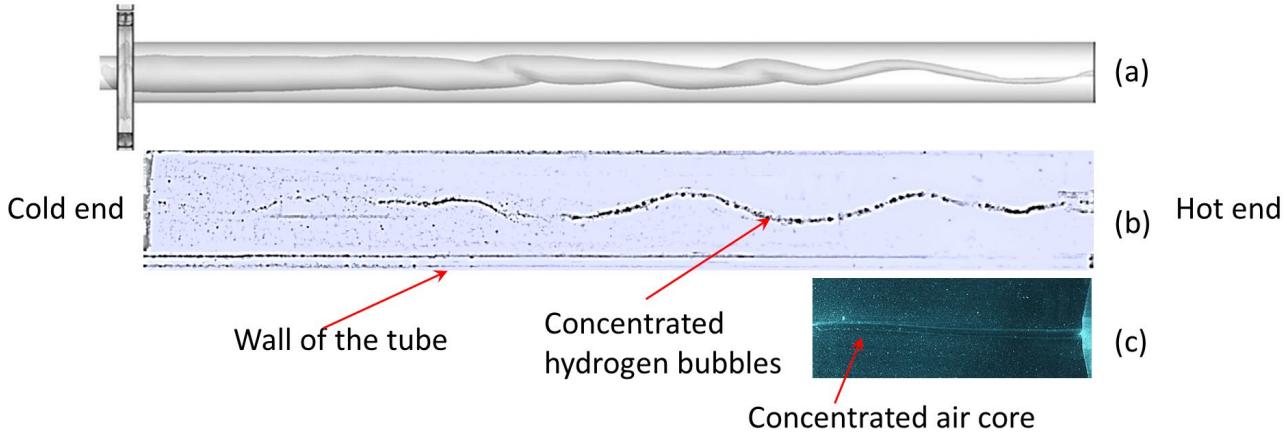

Figure 16. Visualized iso-surface of the instantaneous axial velocity showing the flow structure of the vortex core in a numerical simulation [25] (a); visualized precessing vortex core along the long vortex tube, case "b" (b); concentrated air cone showing the vortex core in the tube, case "c" (c).

A snapshot of the PIV vector (case "b", l/L=0.1) presented in Figure 17 shows the instantaneous location of the vortex core does not coincide with the geometrical centre of the tube. As shown in the figure, two parameters, i.e., the linear and angular displacements of the vortex core were used to evaluate the precession. The displacement of the vortex core (r_{PVC}) is the distance between the vortex core and the geometry centre of the tube and can be used to indicate the strength of the precession. The relative angular displacement (θ_{PVC}) is defined as the angular difference between the "X" axis and the instantaneous location of the vortex core. These two parameters were successfully used to track the vortex core locations in a swirling jet flow [44]. To have better identification of the vortex centre in the instantaneous vector and to identify any coherent structures, a snapshot Proper Orthogonal Decomposition (POD) of the PIV results is performed here. Mode information of the snapshot POD and its mathematical process can be found in [45, 46].

Figure 18 presents the distribution of the contributions from the POD modes to the total energy at different locations of the short tube (case "a"). The lower modes contain most of the energy for the PODs, particularly for l/L=0.125, while the contribution from the higher modes is very small. However, based on the eigenvalues, it is not sufficient to claim any dominating large-scale strongly coherent structures. In other words, it is reasonable to conclude form the eigenvalue distribution that the turbulent flow structure in a short vortex

tube is complex and consisted of small-scale structures. A decrease of the eigenvalues of the lower modes from the cold end to the hot end can be also observed in the figure, which implies the transformation of large-scale fluctuating structure to small-scale turbulent structure along the tube and the similar contribution to the total turbulent energy from different modes.

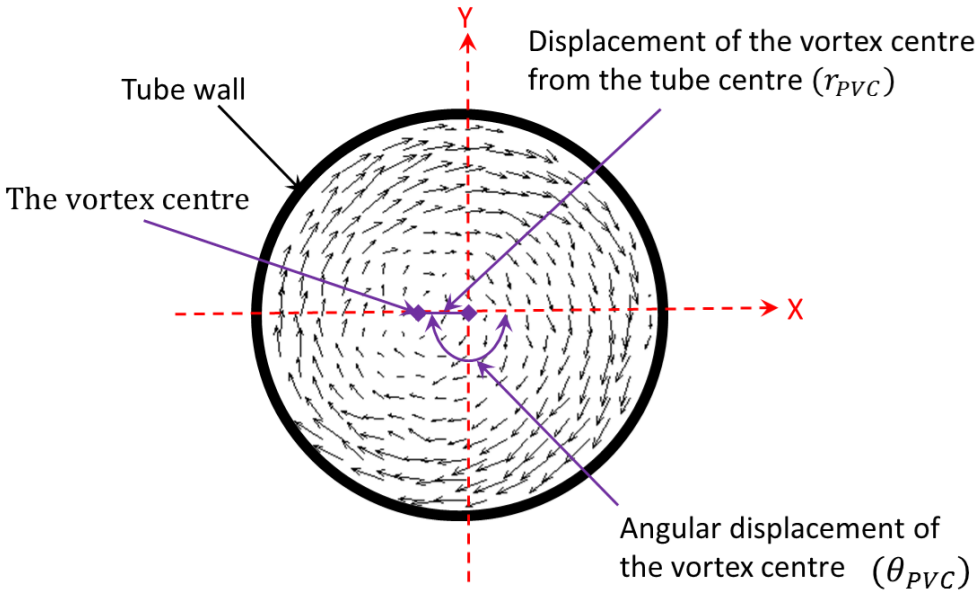

Figure 17. A typical instantaneous PIV vector field at *l/L*=0.1, case "b" shows the offset between the vortex core and the geometrical centre of the tube.

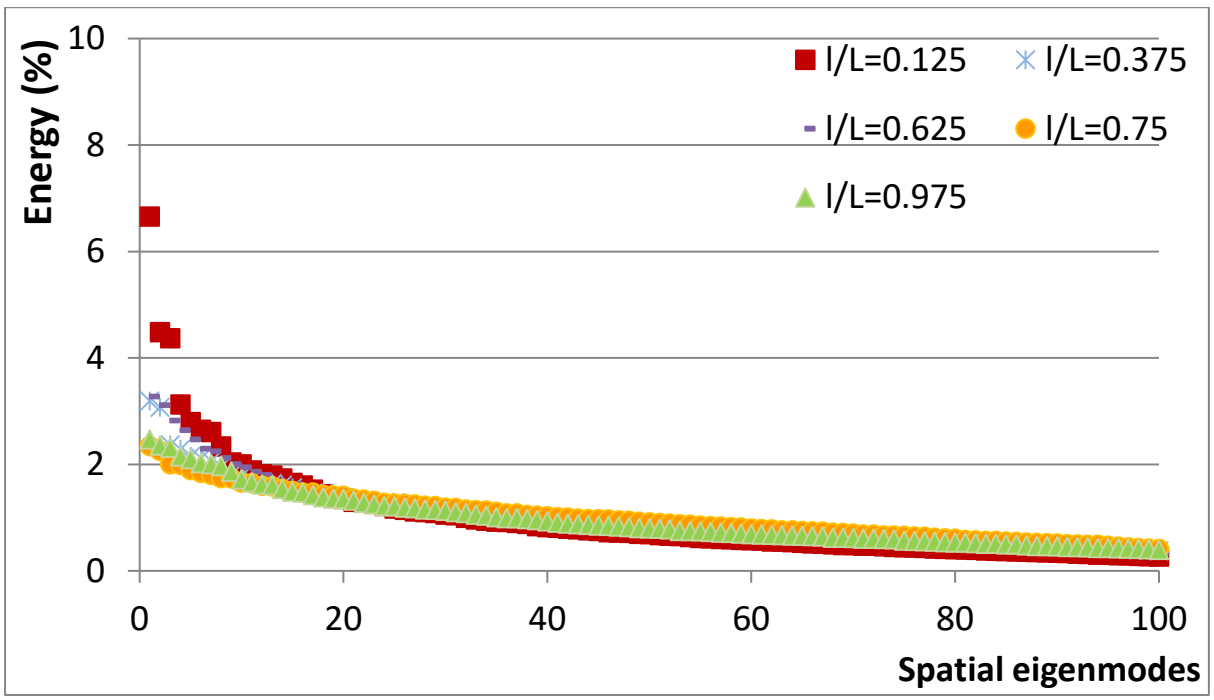

Figure 18. The percentages of the POD eigenvalues in total energy at different location of the short tube (case "a").

Figure 19 presents the distribution of the contributions from the POD modes to the total energy at different locations of the long tube (case "b"). The eigenvalue distribution at *l/L*=0.1 shows dominating large-scale coherent structures with the first two modes contain about 20.4% of the total turbulent energy. With the flow moves to the other of the tube, the decrease of the eigenvalues indicates the dissipation of these large-scale coherent structures.

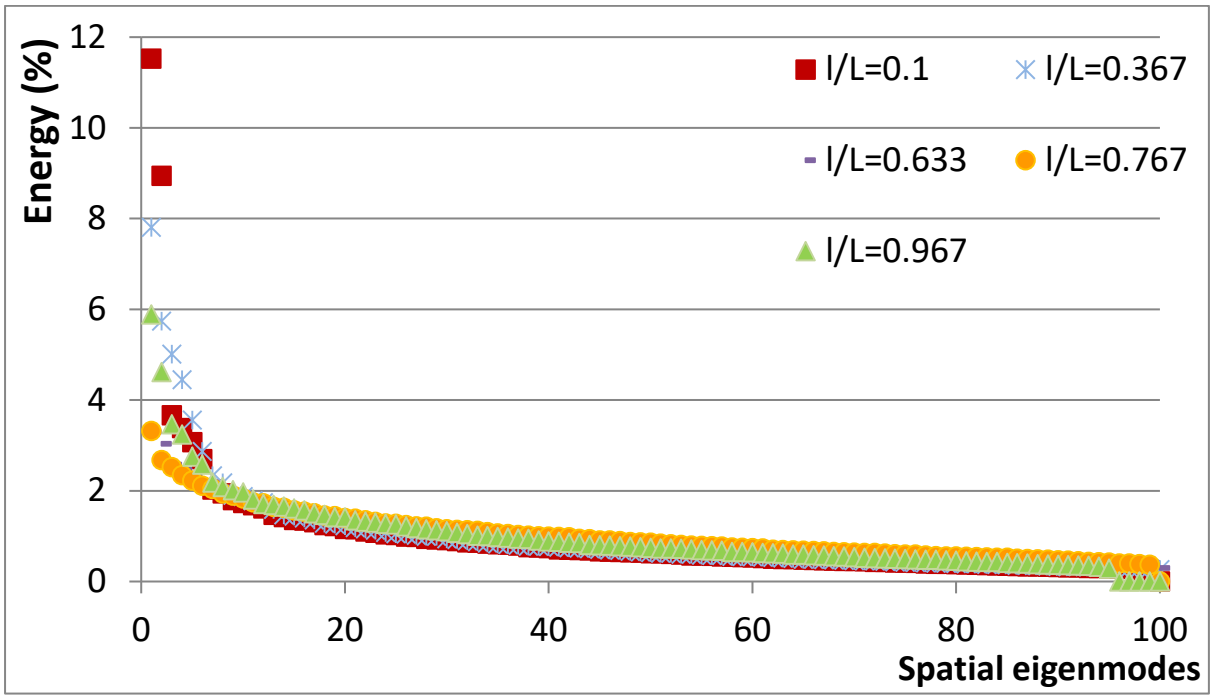

Figure 19. The percentages of the POD eigenvalues in total energy at different location of the short tube (case "b").

The first three modes and the reconstruction of the flow vector are presented in Figure 20. POD modes 1 and 2 shown in figure 20 are significantly stronger than the remaining modes. They each represent 11.5% and 8.9% of the energy in the velocity fluctuations, whereas modes 3 represents only 3.6% and even less for the remaining modes. These two energetic modes are mainly consisted of two vortices and owing to the axisymmetry of the mean flow, mode 2 is obtained from mode 1 by a -90 degree rotation. This is in good agreement with the POD analysis of a vortex flow in a cylinder duct [47]. Based on the first three modes, the velocity filed can be reconstructed as shown in the figure which shows a clearer view of the velocity field by removing the small-scale fluctuations. Figure 21 shows the reconstructed velocity field having a clearer view of the linear and angular displacements of the vortex centre which can improve the identification and location of the vortex centre. According to the eigenvalue distributions, the first ten modes are selected to reconstruct the velocity filed for all the locations and different cases for further detection of vortex position on snapshots and track of vortex in time.

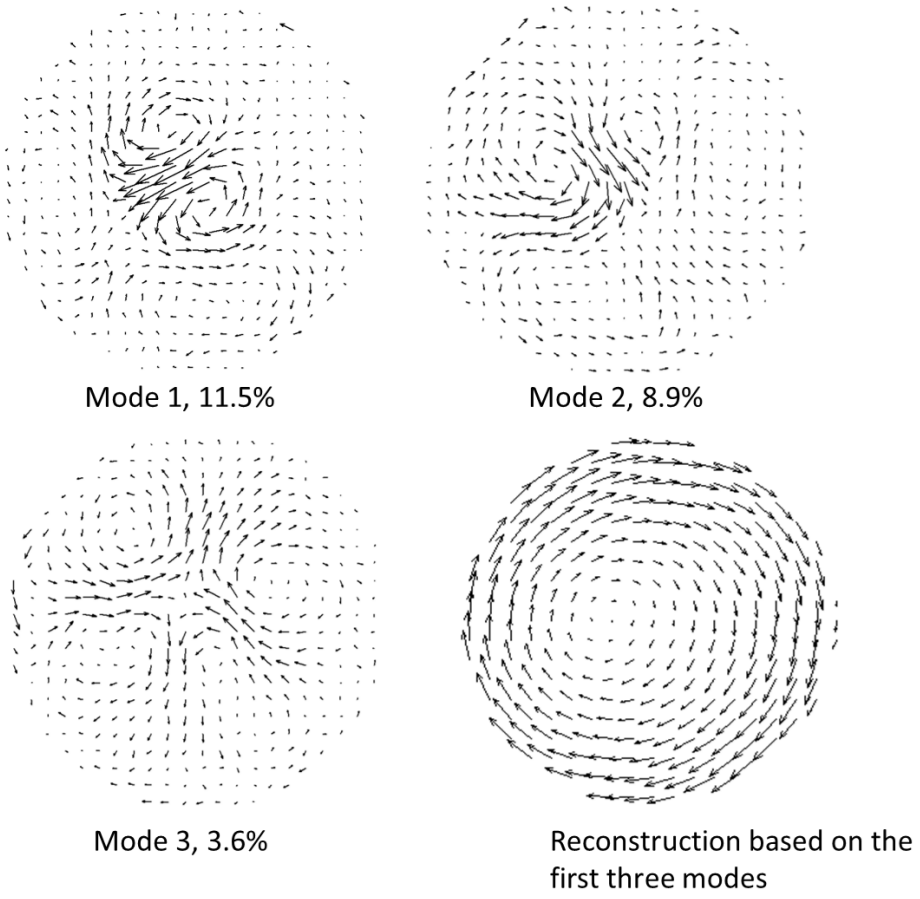

Figure 20. First three POD modes with their eigenvalues and reconstruction of the flow vector based on the first three modes.

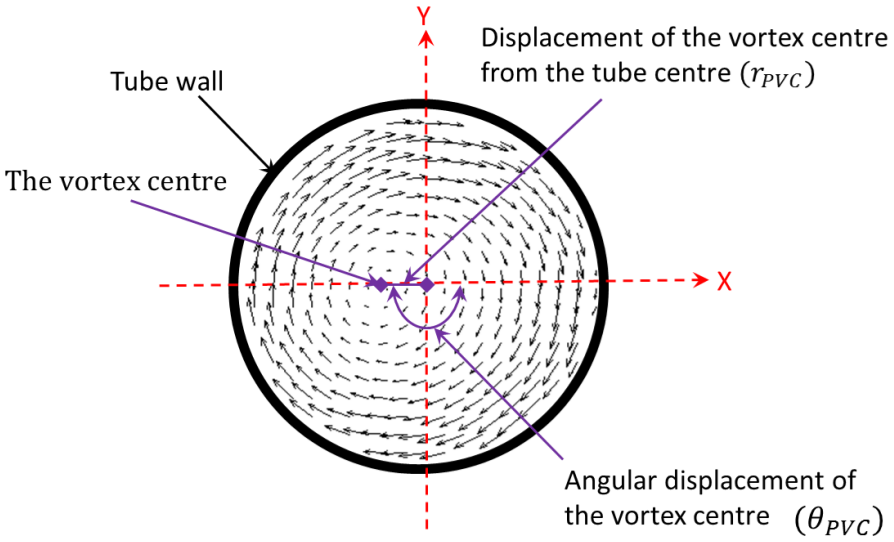

Figure 21. Reconstruction of the velocity vector for vortex centre identification showing a clearer view of the linear and angular displacements of the vortex centre.

Different methodologies have been used to identify the vortex core, such as velocity gradient, vorticity, Q criteria, Δ criteria, and λ_2 criteria [48]. In this work, the velocity gradient is found sufficient to locate the vortex centre in the snapshots and hence obtain the linear and angular

displacement of the vortex centre. Figure 22 presents the time-series of the vortex core angular displacement, relative to the mean location, at l/L=0.1, case "b". As can be seen, the angular displacement appears to fluctuate periodically, which supports the existence of the precession. However, it is also noticed that due to the limited frequency of the laser, direct detection of the PVC in time series from the PIV snapshots is not available in the current work and high frequency time-resolved measurement is required for future investigation.

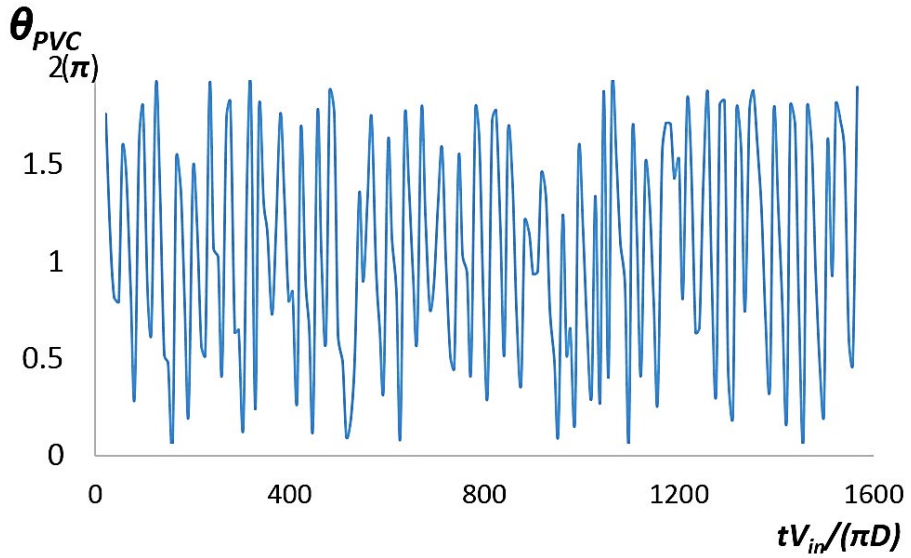

Figure 22: The time-series of the vortex core angular displacement at l/L=0.1, case "b".

The calculated average vortex core radial displacements along the tube (relative to the location of the mean vortex core centre), normalized by the tube diameter, is shown in figure 23. The results clearly show that there is a non-zero value for $\overline{\Delta r_{PVC}}$ throughout the cavity in case "a" and "b", which strongly indicates the existence of the precession. While, in case "c", "d" and "e", the much smaller average vortex core displacements imply the stable swirling flow in these cases. This observation shows a good consistency with the velocity profile and flow visualisation results discussed above. It is also noticed that the average vortex core radial displacements in both case "a" and "b" fluctuate along the tube. In contrast, the displacements in the other three cases are all smaller than 0.02D. This different appearance of the precession is dominated by the swirl velocity profile within the cavity. Swirl number is usually found effective in describing the flow feature of a swirling flow. But in the current case, due to the lack of axial velocity profile and unsteady reverse flow within case "a", "b" and "c", angular velocity of the central flow is used to quantify the swirling flow strength.

The central flow is defined as flow within the region $|r/D| \leq 0.12$ in all cases, except for tube

"c", in which the central flow should be limited in $|r/D| \leq 0.06$. Based on the velocity profiles reported in previous section, the average angular velocity within different tubes are about 6 *rad/s* (case "a"), 12 *rad/s* (case "b"), 120 *rad/s* (case "c"), 0.5 *rad/s* (case "d") and 0.5 *rad/s* (case "e"), respectively. Hence, the frequencies of the swirling flow in these tubes are 0.95, 1.9, 19, 0.079, and 0.079 *Hz*, respectively. Therefore, it can be concluded that the precession of the vortex core is a function of the swirl strength. When the flow is swirling very slowly (case "d" and case "e"), the vortex core in the central region does not oscillate around the geometrical centre but remains steady. When the flow is rotating faster, in order of 10 *rad/s* in this work, the vortex core oscillates around the tube centre with the maximum average displacement of about 0.11D. Once the swirling flow is further strengthened, 120 *rad/s* in case "c", the vortex become centrosymmetric again. This tendency is clearly shown in the top-right figure which is the averaged value of the normalized vortex core offset against the average angular velocity in each case and agrees well with the observed oscillating vortex core at an angular velocity of 40 *rad/s* in an water-operated vortex tube [14] and negligible offset of the vortex core from the tube centre at an angular velocity of 2000 *rad/s* in an air-operated vortex tube [23]. In an industrial vortex tube, the angular velocity varies from 10^4 to 10^5 *rad/s*, which means the vortex flow within the cavity is highly symmetrical. However, the detailed relationship between the vortex flow and the precession of the core, and the influence of this precession on the heat and mass transfer within the vortex tube still require further study.

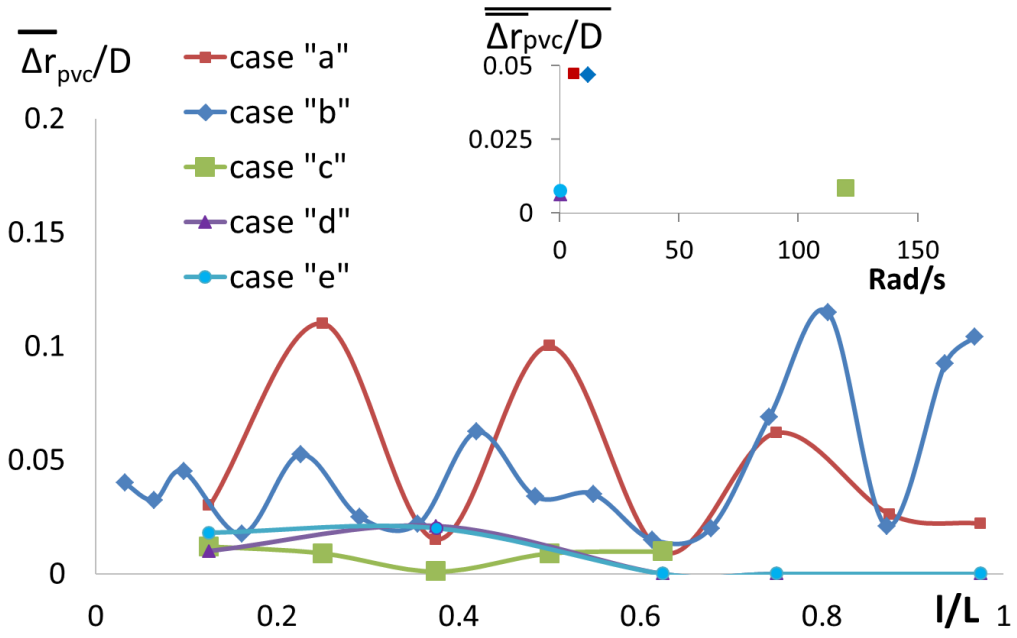

Figure 23: The average vortex core radial displacement along the tube (relative to the mean location) as a function of the nondimensional length of the tube in different cases and the averaged value of the radial displacement as a function of the average angular velocity of each case.

4. Conclusion

The velocity profile within a vortex tube system was investigated in this work. Several transparent tubes were employed to allow flow visualisation and PIV measurement. Different configurations of the tube were selected corresponding to the geometries reported in previous discussion to allow a comparison of the flow behaviour [13]. Both qualitative and quantitative results were obtained and post-processed. The observed flow features in different cases are consistent with the proposed flow mechanism in a vortex tube at different conditions.

The dominating flow feature inside a vortex tube (case “a” and “b”) is found to be a forced vortex and decays towards the hot end. In the central part of the flow in the long vortex tube, a transformation from a forced vortex to a free vortex is observed which is consistent with previously published work [13]. The strength of the central free vortex which flows towards the cold end is controlled by the hot exit, which also controls the cold mass fraction. This central flow plays an important role in transferring energy from inner flow towards the peripheral flow and improving the tube efficiency.

Corresponding to a large cold mass fraction in previous discussion [13], the flow feature in case “c” indicates the dominating free vortex near the hot end and hence results in a smaller scale of the multi-circulation. The existence of the suction of ambient fluid in case “d” and its effect on the flow feature comparing with case “e”, agree well with the flow mechanism within a vortex tube at a small cold mass fraction as discussed in [13].

Snapshot Proper Orthogonal Decomposition is used to evaluate the fluctuating energy associated with vortex and the turbulence kinetic energy excluding the vortex movements. The turbulent flow structures in the short vortex tube and in most of the long tube are found complex and consisted of small-scale structures. A decrease of the eigenvalues of the lower modes from the cold end to the hot end implies the transformation of large-scale fluctuating structure to small-scale turbulent structure along the tube. The reconstructed velocity vector is found helpful to detect and track the vortex centre in time.

The precessing vortex core is clearly observed in the flow visualization and PIV

measurement and agrees well with the previous numerical results [25]. The precession of the vortex core is found a function of the swirl strength. With the strengthening of the swirl, the magnitude of the precession increases to a maximum and then decreases with further strengthening. Further detailed investigation of the PVC in a vortex tube and its impacts on the tube performance is highly recommended.

5. Acknowledgement

The authors acknowledge the support or the ARC Training Centre of Naval Design and Manufacturing (RTCNDM) in this investigation. The RTCNDM is a University-Industry partnership established under the Australian Research Council Industry Transformation grant scheme (ARC IC140100003).

6. Reference

1. Bruno, T.J., *Laboratory applications of the vortex tube.* Journal of Chemical Education, 1987. **64**(11): p. 987.
2. Yalçin, B., A.E. Özgür, and M. Koru, *The effects of various cooling strategies on surface roughness and tool wear during soft materials milling.* Materials and Design, 2009. **30**(3): p. 896-899.
3. Ahmad-Yazid, A., Z. Taha, and I.P. Almanar, *A review of cryogenic cooling in high speed machining (HSM) of mold and die steels.* Scientific Research and Essays, 2010. **5**(5): p. 412-427.
4. Selek, M., et al., *Experimental examination of the cooling performance of Ranque-Hilsch vortex tube on the cutting tool nose point of the turret lathe through infrared thermography method.* International Journal of Refrigeration, 2011. **34**(3): p. 807-815.
5. Liew, R., et al., *Droplet behaviour in a Ranque-Hilsch vortex tube.* Journal of Physics: Conference Series, 2011. **318**(SECTION 5).
6. Crocker, A.M., et al. *Investigation of enhanced vortex tube air separators for advanced space transportation*. in *40th AIAA/ASME/SAE/ASEE Joint Propulsion Conference and Exhibit*. 2004. Fort Lauderdale, FL.
7. Karthikeya Sharma, T., G. Amba Prasad Rao, and K. Madhu Murthy, *Numerical Analysis of a Vortex Tube: A Review.* Archives of Computational Methods in Engineering, 2016: p. 1-30.
8. Eiamsa-ard, S. and P. Promvonge, *Review of Ranque-Hilsch effects in vortex tubes.* Renewable and Sustainable Energy Reviews, 2008. **12**(7): p. 1822-1842.
9. Subudhi, S. and M. Sen, *Review of Ranque-Hilsch vortex tube experiments using air.* Renewable and Sustainable Energy Reviews, 2015. **52**: p. 172-178.
10. Thakare, H.R., A. Monde, and A.D. Parekh, *Experimental, computational and optimization studies of temperature separation and flow physics of vortex tube: A review.* Renewable and Sustainable Energy Reviews, 2015. **52**: p. 1043-1071.
11. Xue, Y., M. Arjomandi, and R. Kelso, *A critical review of temperature separation in a vortex tube.* Experimental Thermal and Fluid Science, 2010. **34**(8): p. 1367-1374.
12. Xue, Y., M. Arjomandi, and R. Kelso, *Energy analysis within a vortex tube.* Experimental Thermal and Fluid Science, 2014. **52**(0): p. 139-145.

13. Xue, Y., M. Arjomandi, and R. Kelso, *The working principle of a vortex tube.* International Journal of Refrigeration, 2013. **36**(6): p. 1730-1740.
14. Xue, Y., M. Arjomandi, and R. Kelso, *Visualization of the flow structure in a vortex tube.* Experimental Thermal and Fluid Science, 2011. **35**(8): p. 1514-1521.
15. Exair, *http://www.exair.com/vortextube/vt*.
16. Gao, C., *Experimental study on the Ranque-Hilsch Vortex Tube*. 2005, Technische Universiteit Eindhoven.
17. Hartnett, J.P. and E.R.G. Eckert, *Experimental study of the velocity and temperature distribution in a high-velocity vortex-type flow.* Trans. ASME, 1957. **79**(4): p. 751-758.
18. Lay, J.E., *An experimental and analytical study of vortex-flow temperature separation by superposition of spiral and axial flow, part I.* Trans. ASME J. Heat Transfer, 1959. **81**: p. 202–212.
19. Lay, J.E., *An experimental and analytical study of vortex flow temperature separation by superposition of spiral and axial flows: Part II.* Trans ASME J Heat Transfer, 1959. **81**(4): p. 202-212.
20. Bruun, H.H., *Experimental Investigation of the Energy Separation in Vortex Tubes.* Journal of Mechanical Engineering Science, 1969. **11**(6): p. 567-582.
21. Takahama, H., *Studies on vortex tubes.* Bull. JSME, 1965. **8**(31): p. 433-440.
22. Ahlborn, B. and S. Groves, *Secondary flow in a vortex tube.* Fluid Dynamics Research, 1997. **21**(2): p. 73-86.
23. Xue, Y., M. Arjomandi, and R. Kelso, *Experimental study of the flow structure in a counter flow Ranque–Hilsch vortex tube.* International Journal of Heat and Mass Transfer, 2012. **55**(21–22): p. 5853-5860.
24. Xue, Y., M. Arjomandi, and R. Kelso, *Experimental study of the thermal separation in a vortex tube.* Experimental Thermal and Fluid Science, 2013. **46**: p. 175-182.
25. Guo, X. and B. Zhang, *Computational investigation of precessing vortex breakdown and energy separation in a Ranque–Hilsch vortex tube.* International Journal of Refrigeration, 2018. **85**: p. 42-57.
26. Zhang, B., X. Guo, and Z. Yang, *Analysis on the fluid flow in vortex tube with vortex periodical oscillation characteristics.* International Journal of Heat and Mass Transfer, 2016. **103**: p. 1166-1175.
27. Liew, R., et al., *Temperature, Pressure and Velocity measurements on the Ranque-Hilsch Vortex Tube.* Journal of Physics: Conference Series, 2012. **395**(1): p. 012066.
28. Liew, R., et al., *3D Velocimetry and droplet sizing in the Ranque–Hilsch vortex tube.* Experiments in Fluids, 2013. **54**(1): p. 1-16.
29. Xue, Y., M. Arjomandi, and R. Kelso, *Experimental study of the flow structure in a counter flow Ranque-Hilsch vortex tube.* International Journal of Heat and Mass Transfer, 2012. **55**(21-22): p. 5853-5860.
30. Liu, Z., et al., *Stereoscopic PIV studies on the swirling flow structure in a gas cyclone.* Chemical Engineering Science, 2006. **61**(13): p. 4252-4261.
31. Chiné, B. and F. Concha, *Flow patterns in conical and cylindrical hydrocyclones.* Chemical Engineering Journal, 2000. **80**(1-3): p. 267-273.
32. Hoekstra, A., J. Derksen, and H. Van Den Akker, *An experimental and numerical study of turbulent swirling flow in gas cyclones.* Chemical Engineering Science, 1999. **54**(13-14): p. 2055-2065.
33. Adrian, R.J. and J. Westerweel, *Particle Image Velocimetry*. 2011: Cambridge University Press, Cambridge, UK.
34. Squire, D.T., et al., *Comparison of turbulent boundary layers over smooth and rough surfaces up to high Reynolds numbers.* Journal of Fluid Mechanics, 2016. **795**: p. 210-240.
35. Secchiaroli, A., et al., *Numerical simulation of turbulent flow in a Ranque-Hilsch vortex tube.* International Journal of Heat and Mass Transfer, 2009. **52**(23-24): p. 5496-5511.

36. Hoekstra, A.J., J.J. Derksen, and H.E.A. Van Den Akker, *An experimental and numerical study of turbulent swirling flow in gas cyclones.* Chemical Engineering Science, 1999. **54**(13): p. 2055-2065.
37. Bai, Z.-s., H.-l. Wang, and S.-T. Tu, *Experimental study of flow patterns in deoiling hydrocyclone.* Minerals Engineering, 2009. **22**(4): p. 319-323.
38. Chiné, B. and F. Concha, *Flow patterns in conical and cylindrical hydrocyclones.* Chemical Engineering Journal, 2000. **80**(1–3): p. 267-273.
39. Kurosaka, M., *Acoustic streaming in swirling flow and the Ranque—Hilsch (vortex-tube) effect.* Journal of Fluid Mechanics, 1982. **124**( ): p. 139-172.
40. Syred, N., *A review of oscillation mechanisms and the role of the precessing vortex core (PVC) in swirl combustion systems.* Progress in Energy and Combustion Science, 2006. **32**(2): p. 93-161.
41. Wu, X. and M. Shi, *Visualization of the precessing vortex core in a cyclone sepaarator by PIV.* Chinese J. Chem. Eng., 2003. **11**(6): p. 633-637.
42. Cullivan, J.C., et al., *New understanding of a hydrocyclone flow field and separation mechanism from computational fluid dynamics.* Minerals Engineering, 2004. **17**(5): p. 651-660.
43. Zou, J., C. Wang, and C. Ji, *Experimental study on the air core in a hydrocyclone.* Drying Technology, 2016. **34**(7): p. 854-860.
44. Martinelli, F., A. Olivani, and A. Coghe, *Experimental analysis of the precessing vortex core in a free swirling jet.* Experiments in Fluids, 2007. **42**(6): p. 827-839.
45. Sirovich, L., *Turbulence and the dynamics of coherent structures. I. Coherent structures.* Quarterly of applied mathematics, 1987. **45**(3): p. 561-571.
46. Meyer, K.E., J.M. Pedersen, and O. Özcan, *A turbulent jet in crossflow analysed with proper orthogonal decomposition.* Journal of Fluid Mechanics, 2007. **583**: p. 199-227.
47. Graftieaux, L., M. Michard, and N. Grosjean, *Combining PIV, POD and vortex identification algorithms for the study of unsteady turbulent swirling flows.* Measurement Science and technology, 2001. **12**(9): p. 1422.
48. Epps, B., *Review of Vortex Identification Methods*, in *55th AIAA Aerospace Sciences Meeting*. 2017, American Institute of Aeronautics and Astronautics.